


Material design for hydraulic silencers

Dongwei Wang,¹ Binghao Zhao^{1,†}, Yu Wei^{1,†}, Jun Yang,² and Gengkai Hu^{1,*}

¹*School of Aerospace Engineering, Beijing Institute of Technology, Beijing 100081, China*

²*Shenzhen Institute for Advanced Study, University of Electronic Science and Technology of China, Shenzhen 518110, China*

 (Received 12 June 2024; revised 11 August 2024; accepted 13 August 2024; published 4 September 2024)

Mitigation of fluid-borne noise in hydraulic power systems is of paramount importance for both machine reliability and human comfort. One typical approach involves using compliant inline hydraulic silencers to lower the sound speed within devices, e.g., pressurized bladders or syntactic foams. However, the exploration of innovative compliant materials for silencer designs has been limited; this is largely due to the absence of a comprehensive model that can accommodate a large range of anisotropic materials to evaluate the performance of hydraulic silencers. In this work, we develop a general analytical model for silencer design that incorporates anisotropic reflective materials. The model enables us to identify optimized solutions within a broader material spectrum, tailored to meet pressure-resistance requirements. Building upon these insights, we design and fabricate an anisotropic compliant metallic lattice with low impedance and integrate it into a hydraulic silencer as the reflective material. Experimental results demonstrate that this silencer can achieve an average sound-transmission loss of 21 dB across a frequency range of 100 Hz to 2 kHz, in good agreement with predictions from our proposed model. This work paves the way for selecting and designing innovative materials for the mitigation of hydraulic noise.

DOI: [10.1103/PhysRevApplied.22.034010](https://doi.org/10.1103/PhysRevApplied.22.034010)

I. INTRODUCTION

Noise reduction in hydraulic circuits is of significant importance in various circumstances, including industrial settings, architectural structures, vehicular environments, and maritime equipment. Within these systems, pressure ripples (also known as fluid-borne noise) originating from engines or pumps, propagate through pipeline circuits. This noise can either couple with structural components of the system to vibrate these components and emit air-borne noise or ultimately interfere with downstream critical apparatus [1–3]. Hence, hydraulic silencers assume a pivotal role to mitigate and manage the impact of these invasive noise disturbances.

Passive silencers are commonly employed to reduce noises in pipeline systems, including three major types: resistive, reactive, and hybrid [4]. Among these, resistive silencers employ absorptive materials to attenuate sound energy. Commonly utilized absorptive elements include fibrous materials [5,6] and perforated plates [7,8], either individually or in combination [9–11], to fulfill the required functions. However, their effectiveness experiences a notable decline when tackling fluid-borne

sound-absorption challenges, especially in the low-frequency range [12].

Reactive silencers utilize impedance change, driven by either resonances or compliant materials, to suppress noise in upstream regions, proving particularly effective in the low-to-moderate-frequency spectrum [13]. Resonant-style reactive silencers, including Quincke tubes [14,15] and Helmholtz resonators [9,16,17], use resonant mechanisms to create a condition of zero impedance. However, their narrowband and relatively large volume (inversely proportional to frequency) limit their practical applications. In contrast, compliant-style reactive silencers achieve impedance mismatches by creating cross-section discontinuity or altering the material's properties along flow paths [13]. A typical example of cross-section discontinuity is the use of expansion chambers, resulting in a characteristic dome-shaped curve of sound-transmission loss (STL) [4]. Evolving from basic expansion chambers, numerous chamber-type structures have been developed to enhance acoustic insulation performance, including multichamber configurations [18–21], extended-duct chambers [22,23], and reflective liner designs [6,9]. Among these, appropriate liner materials can significantly enhance their sound-mitigation performance. Huang [24,25] introduced an elastic membrane inside the chamber to replace the duct wall of an air pipeline, creating destructive interference between the straight downstream waves and the radiated waves from the membrane [24]. Extending this

*Contact author: hugeng@bit.edu.cn

†Also at School of Chemical Engineering, Ocean and Life Sciences, Dalian University of Technology, China.

concept to fluid-borne sound, researchers have designed bladder-type suppressors by filling air in cavities to ensure significant impedance mismatch [26]. Nonetheless, essential maintenance is required to regulate air pressure in the bladder. Hybrid silencers, employing both resistant and reactive mechanisms to fulfill broadband sound insulation and absorption [10,11,26], also face similar problems.

A potential approach to circumvent the above difficulties in hydraulic silencer design may involve employing a solid material that possesses both low impedance and sufficient stiffness as a reflective material. For instance, Pedigo and Cunefare [27] proposed utilizing syntactic foams to replace bladders; in their case, the nonlinear behavior of these foams played a critical role due to buckling of hollow microspheres under pressure. Typically, in a linear regime, it is difficult to have low impedance and high stiffness simultaneously due to their positive correlation for isotropic materials, i.e., low impedance definitely means low stiffness [28]. Recently, a kind of specific anisotropic material has shown potential to decouple this correlation, allowing for the design of materials with low impedance and adequate stiffness as well. Chen *et al.* [29] and Wang *et al.* [30] proposed a low-impedance anisotropic pentamode material tailored specifically to insulate low-frequency fluid-borne sound, even under oblique incident conditions. Therefore, incorporating anisotropic solid compliant materials into hydraulic silencer design appears promising. However, existing research has mainly focused on isotropic fluidlike materials like inflatable bladders, rubber, or foam [5,6,26]. Studies on anisotropic solid materials are lacking due to the complexity of wave propagation within these materials. In this work, we aim to establish a general theoretical model for inline hydraulic silencers with anisotropic materials, with the hope of enlarging the material selection space for innovative compliant material design.

This paper is organized as follows: Sec. II establishes a theoretical model of a typical silencer with general anisotropic materials. An optimization to find optimal reflective materials is conducted in Sec. III; the underlying mechanism of sound insulation of the silencer is also presented. The optimal anisotropic material is a kind of pentamode material, and its microstructure design is given in this section. Section IV discusses experimental samples and measurements of the inline hydraulic silencer with the anisotropic material. Finally, Sec. V summarizes the conclusions of the study.

II. THEORETICAL MODEL OF A SILENCER WITH ANISOTROPIC MATERIALS

A. Wave propagation in a silencer with anisotropic materials

The existing models for evaluating the sound-insulating performance of silencers are based on isotropic fluidlike

materials; here, we extend the models to include general anisotropic materials. Consider a two-dimensional (2D) inline silencer with anisotropic materials, as illustrated in Fig. 1. The internal fluid medium (water) is assumed to be quasistationary, and the effects of flow are not considered. Waves propagate along a pipe with different square cross sections, labeled as A, B, and C, with respective heights of $2y_1$, $2y_2$, and $2y_1$. Two identical plates of anisotropic reflective material, denoted as D, with length L and height d , symmetrically line the top and bottom sides of chamber B.

Under the assumption of low and steady flow within pipes, the acoustic wave pressure at inlet A can be expressed as a combination of a planar incident wave and reflected harmonic waves as [5]

$$P_A(x, y) = I_{A0} e^{-jk_{xA0}x} \psi_{A0}(y) + \sum_{n=0}^{\infty} R_{An} e^{jk_{xA_n}x} \psi_{An}(y), \quad (1)$$

where I and R denote the amplitudes of traveling waves in forward and backward directions (with respect to x), respectively. k is the wave number. $\psi(y)$ signifies the modal of the pipe. Subscripts x , A , and n refer to the x axis, region A, and the n th mode, respectively, and are used throughout the paper. The time harmonic term, $e^{-j\omega t}$, is omitted. With the assumption of a planar incident wave, only the zeroth-order incident wave is considered. With symmetric square-crossing sections and rigid-wall boundary conditions, i.e., $\partial P/\partial y = 0$ at $y = \pm y_1$, $\psi_{An}(y)$ is determined by

$$\psi_{An}(y) = \cos(k_{yAn}y), \quad (2)$$

where $k_{yAn} = n\pi/y_1$ is the wave number along the y axis.

In a similar manner, the wave pressures in regions B and C are expressed, respectively, as

$$\begin{aligned} P_B(x, y) &= \sum_{n=0}^{\infty} (I_{Bn} e^{-jk_{xBn}x} + R_{Bn} e^{jk_{xBn}x}) \psi_{Bn}(y), \\ P_C(x, y) &= \sum_{n=0}^{\infty} I_{Cn} e^{-jk_{xCn}(x-L)} \psi_{Cn}(y), \end{aligned} \quad (3)$$

where $\psi_{Bn}(y) = \cos(k_{yBn}y)$ and $\psi_{Cn}(y) = \cos(k_{yCn}y)$. The component of the wave number is given for $k_{yCn} = n\pi/y_1$. However, k_{yBn} should be determined by the interaction with the anisotropic material in region D. All components of the wave number in water follow the following relationship:

$$k_{xin}^2 + k_{yin}^2 = k_0^2, \quad i = A, B, C, \quad (4)$$

with $k_0 = \omega/c_0$, where ω is the angular frequency.

The displacements within the reflective anisotropic material (region D) can be obtained by superposing the

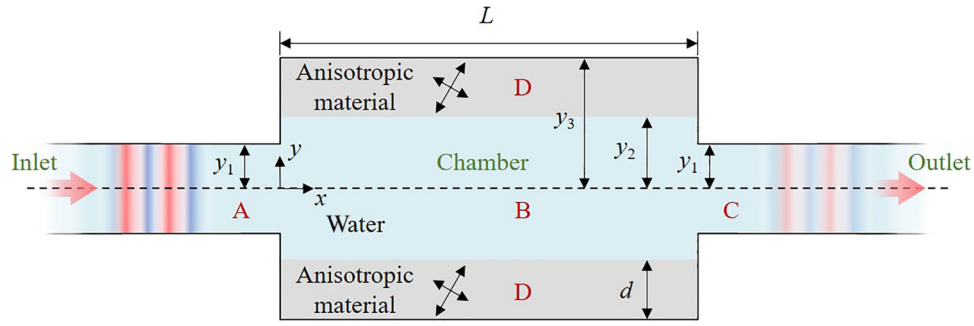


FIG. 1. Sketch of a 2D inline silencer with anisotropic materials.

contributions of waves excited by forward and backward incident waves (with respect to x), as illustrated in Fig. 2. For the forward incident wave, four elastic waves, as indicated by the red lines in Fig. 2, will propagate within the anisotropic plate: two quasilongitudinal and two quasitransversal waves, with one of each type moving in the upward direction and the other pair in the downward direction. The magenta double-headed arrows indicate the polarization directions of these waves.

The total displacement components are expressed as

$$\mathbf{u}_n = \sum_{\alpha=1}^4 I_{Bn} u_{n\alpha}^+ \begin{Bmatrix} m_{n\alpha}^+ \\ n_{n\alpha}^+ \end{Bmatrix} e^{-j(k_x B_n x + k_y \alpha n y)} + R_{Bn} u_{n\alpha}^- \begin{Bmatrix} m_{n\alpha}^- \\ n_{n\alpha}^- \end{Bmatrix} e^{j(k_x B_n x + k_y \alpha n y)}. \quad (5)$$

The detailed derivation is provided in Appendix A. It is noted that the plane-strain assumption is applied in both the theoretical analysis and subsequent numerical simulations. Additionally, unlike isotropic materials, the displacement amplitudes for the opposite incident wave numbers generally differ due to the asymmetry of principal axes. This feature adds to the complexity of the analytical model.

Notably, the method can also be applied to the case of a fluid medium by setting

$$u_{n1}^{\pm} = \frac{I_B k_D C_1}{j \rho_D \omega^2}, \quad u_{n2}^{\pm} = \frac{I_B k_D C_2}{j \rho_D \omega^2}. \quad (6)$$

In this case, only longitudinal waves exist within the fluid (assuming density ρ_D and wave number k_D). The corresponding pressure within the medium is represented as

$$\tilde{P}_D(x, y) = \sum_{n=0}^{\infty} (I_{Bn} e^{-j k_x B_n x} + R_{Bn} e^{j k_x B_n x}) (C_1 e^{-j k_y D_n y} + C_2 e^{j k_y D_n y}). \quad (7)$$

The forward and backward waves take the same transversal mode component, which is essentially different from anisotropic materials.

B. Sound-transmission loss of the silencer

To address the governing equations of the silencer, axial matching conditions between different regions are necessary, which facilitate the continuity and transition of acoustic waves through its various sections. Two primary methodologies are typically employed in constructing these matching conditions for silencers with isotropic materials, such as bladders or dissipative-compliant materials: the direct integration procedure and the standard mode-matching method. The former involves integrating the axial wave velocities at geometrical discontinuities, which is effective for silencers without expansions [6]. The latter method utilizes a weighted integration over cross-section areas, employing the transverse modes of ducts as the weighting function [5]. Due to expanded region B of the silencer under consideration, the standard mode-matching method is utilized and extended to anisotropic material cases.

The governing equations of the silencer can be expressed in matrix form as $\mathbf{A}\mathbf{X}=\mathbf{B}$, where \mathbf{X} is the unknown vector composed of the wave amplitudes R_{An} , I_{Bn} , R_{Bn} , and I_{Cn} . \mathbf{A} is the coefficient matrix derived from the axial matching conditions, and \mathbf{B} is the vector containing the incident-wave amplitudes, I_{An} . The detailed derivation is provided in Appendix B. By solving the governing equations, the sound-transmission loss L_{st} of the silencer can then be evaluated by

$$L_{st} = -20 \log_{10} |I_{C0}|. \quad (8)$$

Other waves corresponding to nonzero modes within region C are evanescent, and they do not contribute to further transmission.

C. Numerical validation of the model

To validate the proposed model, a lightweight general anisotropic material, wood, with specified material properties (modulus $E_1=6.2$ GPa, $E_2=G=0.3$ GPa, density $\rho=0.18$ g/cm³, and Poisson ratio $\nu_{12}=0.23$) is selected for region D. The geometric parameters of the

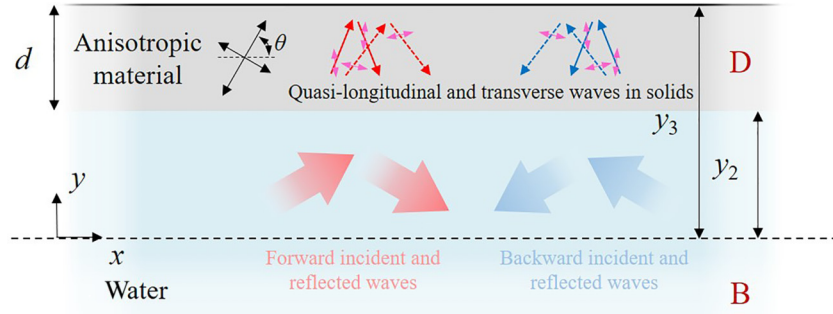


FIG. 2. Fluid-solid interaction in anisotropic plate excited by forward (blue) and backward (red) incident waves.

silencer include $y_1 = 0.04$ m, $y_2 = 0.05$ m, $y_3 = 0.08$ m, and $L = 0.12$ m. The STL curves of the silencer with different rotational angles of the material's principal axis are depicted in Fig. 3(a), exhibiting domelike shapes. Notably, the convergence of the model confirms that the model stabilizes at $N = 5$, as shown in the inset of Fig. 3(a). Additionally, to validate the model, numerical simulations are also conducted using the finite-element method (FEM) with COMSOL Multiphysics, showcasing good agreement with theoretical predictions. The deviations between the theoretical and numerical results in the high-frequency range are mainly attributed to the simplified assumptions made in the theoretical analysis. Specifically, the waves in the fluid are assumed to be planar waves, whereas they actually exhibit curved wavefronts at high frequencies. Additionally, the wave modes in the solid plate are represented by superposing wave displacements, which may differ from the exact modes with complex boundary conditions in the simulations, especially at high frequencies. Details of the setup for numerical simulations are provided in Appendix C.

To figure out the influence of the properties of the anisotropic material on impedance and load-bearing capacity, the elasticity matrix in the principal coordinate

system is expressed as [27]

$$\mathbf{C} = \begin{bmatrix} \Lambda & \gamma & 0 \\ \gamma & \Lambda^{-1} & 0 \\ 0 & 0 & \mu \end{bmatrix} \sqrt{C_{11}C_{22}}, \quad (9)$$

where $\Lambda = \sqrt{C_{11}/C_{22}}$ represents the anisotropy of the material; $\gamma = C_{12}/\sqrt{C_{11}C_{22}}$ ($\gamma \leq 1$) and $\mu = C_{66}/\sqrt{C_{11}C_{22}}$ relate to easy deformation modes [27]. These parameters for the wood studied above are easily calculated as follows: $\Lambda = 4.55$, $\gamma = 0.05$, and $\mu = 0.22$. The impedance of the anisotropic materials is given by [29]

$$Z = \eta \rho c_L, \quad \eta = \frac{1 + \tan^2 \theta}{1 + (c_L/c_T) \tan^2 \theta}, \quad (10)$$

where c_L and c_T denote wave velocities of quasilongitudinal and transversal waves, respectively. The impedance depends additionally (compared to isotropic materials) on parameter η , which can be used to lower the impedance by reducing c_T subjected to the condition $\theta \neq 0^\circ$ (with the ideal case $c_T = 0$).

The variation curves of the effective impedance and vertical modulus along the y axis, i.e., $E_y = 1/\mathbf{C}^{-1}(2, 2)$ as

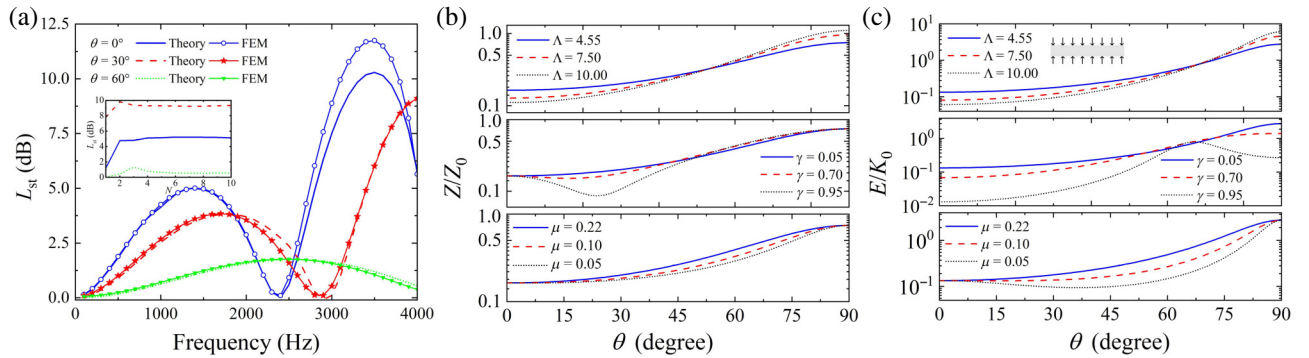


FIG. 3. (a) STL curves as a function of frequency with different rotational angles of the material's principal axis, calculated by FEM and theoretical model. (b) Normalized impedance and (c) vertical modulus as a function of rotational angle of the material's principal axis, with different Λ , γ , and μ .

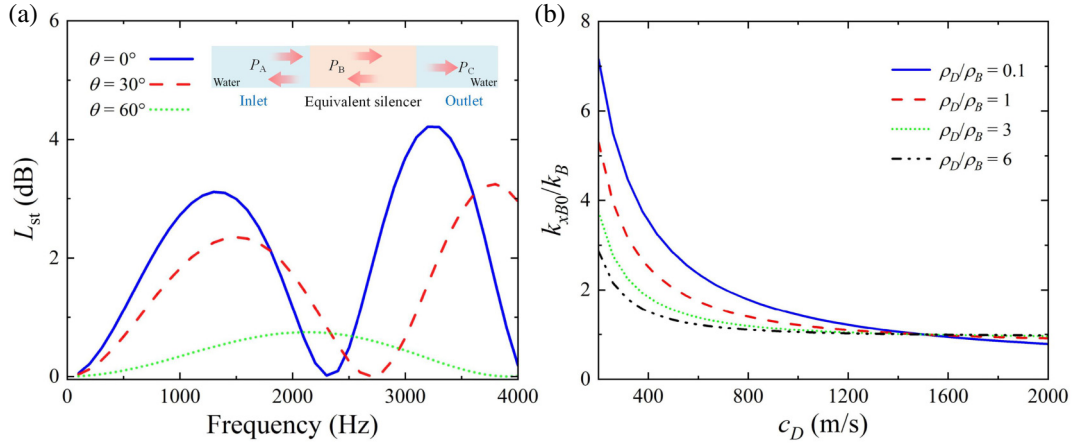


FIG. 4. (a) STL of the simplified silencer. (b) Effects of wave velocity and density on the relative axial wave number for the simplified silencer.

a function of θ , with different Λ , γ , and μ are plotted in Figs. 3(b) and 3(c), respectively. Obviously, a larger anisotropy parameter Λ leads to smaller values of both impedance and modulus. As γ approaches one, the usual monotonic relationship between impedance and modulus breaks down, an effect not available in isotropic materials. It is concluded that a strongly anisotropic material with $\gamma \approx 1$ and $\mu \approx 0$ can realize a remarkably low impedance at a specific rotation angle of the principal axis. This capability demonstrates the potential of using highly anisotropic materials in hydraulic silencer designs.

D. Sound-insulation mechanism of anisotropic silencers

Silencers function by creating a mismatch in the wave number along the axial direction, leading to a reflection of upstream sound waves. To comprehensively understand this mechanism, we extract the axial wave number of the plane wave (0th order) within the silencer and roughly simplify the silencer as an isotropic liquid layer based on these axial wave numbers. The STL of this three-layer model, as shown in the inset of Fig. 4(a), can be easily calculated by [31]

$$L_{st} = -10 \log_{10} \frac{1}{1 + \frac{1}{4} (Z_{B0}/Z_0 - Z_0/Z_{B0})^2 \sin^2 k_{yB0} L}, \quad (11)$$

where Z_{B0} is the equivalent impedance of the simplified silencer in the three-layer model. Even though the high-order harmonic waves are neglected, the trends observed in the STL curves [Fig. 4(a)] remain consistent with those of the complete model. This approximation effectively confirms the reflection mechanism of silencers. Therefore, it can be inferred that sound insulation is predominantly determined by the mismatch of axial wave numbers. This

fundamental principle offers a straightforward yet powerful direction for designing efficient silencers.

The presence of silencers disrupts the one-dimensional waveguide state within the pipeline, introducing additional transversal wave numbers and creating a mismatch in axial wave numbers. In this context, the correlation between the reflective material and the mismatch of the axial wave number must be explored. Given the complexity of analyzing the silencer with general anisotropic materials, we focus on discussing the case with liquid-compliant materials, which is believed to provide a clearer analytical understanding. Considering the interface between regions B and D, the boundary conditions, i.e., Eqs. (3) and (7), are reduced to

$$\begin{aligned} e^{-j k_{yBn} y_2} + e^{j k_{yBn} y_2} &= C_1 e^{-j k_{yDn} y_2} + C_2 e^{j k_{yDn} y_2}, \\ \frac{k_{yBn}}{\rho_B} (e^{-j k_{yBn} y_2} - e^{j k_{yBn} y_2}) &= \frac{k_{yDn}}{\rho_D} (C_1 e^{-j k_{yDn} y_2} - C_2 e^{j k_{yDn} y_2}), \\ C_1 e^{-j k_{yDn} y_3} - C_2 e^{j k_{yDn} y_3} &= 0. \end{aligned} \quad (12)$$

Then the governing equation can be derived as

$$\frac{k_{yBn}}{\rho_B} \tan(k_{yBn} y_2) = j \frac{k_{yDn}}{\rho_D} \frac{e^{2j k_{yDn} y_3} - e^{2j k_{yDn} y_2}}{e^{2j k_{yDn} y_3} + e^{2j k_{yDn} y_2}}. \quad (13)$$

The available axial wave numbers can be calculated for given frequencies. As illustrated in Fig. 4(b), the disparities in the axial wave number of the zeroth order are computed across various relative densities. It is observed that lower values of sound speed and density, which correspond to lower impedance, result in a larger mismatch in impedance. This mechanism for silencers with anisotropic materials is similar to the isotropic case and is indirectly unveiled in the following subsection.

III. MATERIAL OPTIMIZATION AND DESIGN FOR A HYDRAULIC SILENCER

A. Material optimization

According to governing Eqs. (A1)–(A4) in Appendix A, four elastic parameters (C_{11} , C_{12} , C_{22} , C_{66}) in its principal coordinate system, along with rotational angle θ of the principal axis, will determine directly available axial wave numbers in silencers. The matrix in the global system is then computed by $\mathbf{C}_\theta = \mathbf{N}\mathbf{C}\mathbf{N}^T$, where \mathbf{N} is a function of θ , denoting the coordinate transformation matrix [28]. To find an optimal material for a hydraulic silencer, an optimization method based on a genetic algorithm is employed.

Compliant materials with different pressure-resistance capacities are optimized and listed in Table I. More details of this process can be found in Appendix D. All these optimal materials possess similar characteristics: a very small shear modulus; C_{12} is approximately equal to $\sqrt{C_{11}C_{22}}$, i.e., $\gamma \approx 1$; one eigenvalue of the elastic matrix is orders of magnitude larger than the others, which is called a 2D pentamode material, i.e., a single quasinonzero normalized eigenvalue [32]. For example, in case 1, the three normalized eigenvalues of its elastic matrix are given by

TABLE I. Parameters for optimized anisotropic compliant materials.

Case	C_{11}/K_0	C_{12}/K_0	C_{22}/K_0	C_{66}/K_0	θ (deg)	E_y (MPa)
1	1.80	0.13	0.010	0.006	14.90	3.4
2	2.80	0.33	0.041	0.007	15.34	5.5
3	3.06	0.27	0.029	0.013	16.10	13.6
4	2.30	0.25	0.035	0.012	17.19	20.0

(0.0003, 0.003, 1). The small shear-wave velocity and nonzero rotational angle of the principal axis lead to low impedance, which is consistent with Eq. (10). The corresponding STLs for this case are plotted in Fig. 5(a), showcasing an average of 29.0 dB. Numerical simulations by FEM are also conducted, demonstrating satisfactory agreement with the theoretical result. Other cases, as depicted in Fig. 5(b), show that the acoustic performance generally decreases as the pressure-resistance requirement increases.

In addition, the impedance of the optimal material reaches its minimum at the optimized rotational angle, where the material can achieve a remarkably low impedance while maintaining a necessary modulus, as indicated by the dotted black line in Fig. 5(c). To further

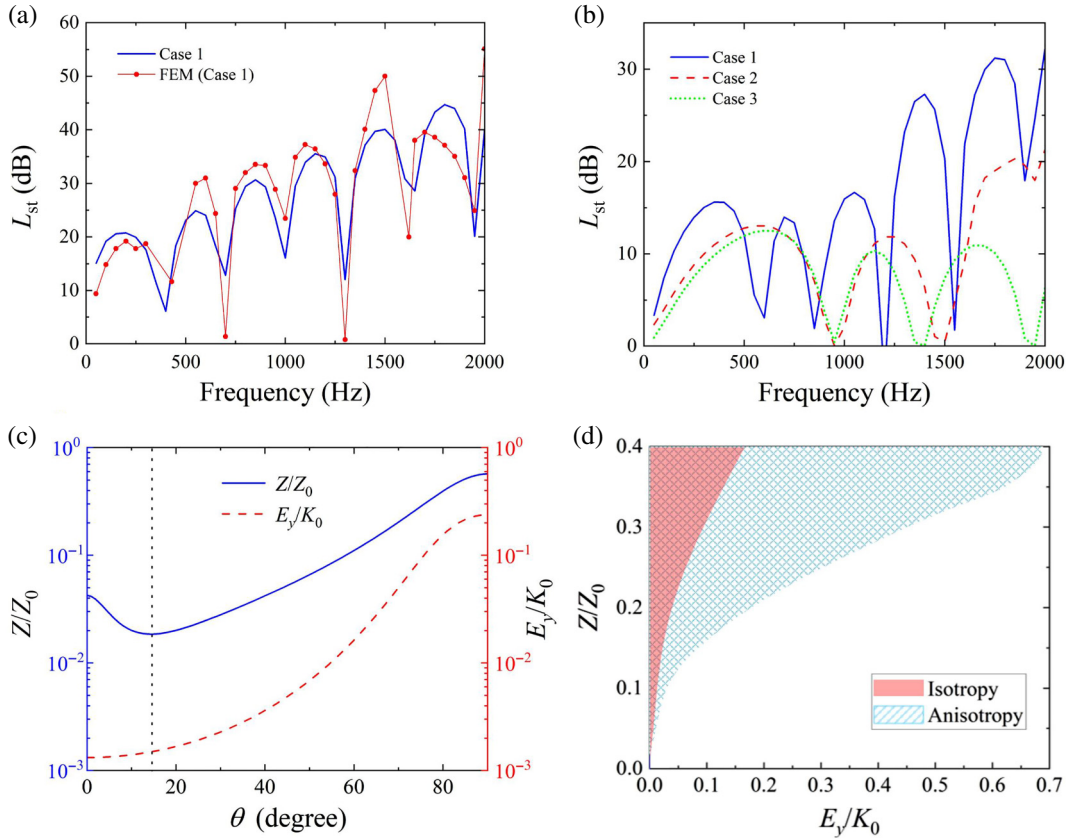


FIG. 5. (a) STL of the silencer with the optimal material in case 1 calculated by FEM and theoretical models. (b) STL of the silencers in cases 2–4. (c) Normalized impedance and modulus of the optimal material in case 1 as a function of rotational angle of the principal axis. (d) Attainable material space for normalized impedance and modulus for isotropic and anisotropic materials.

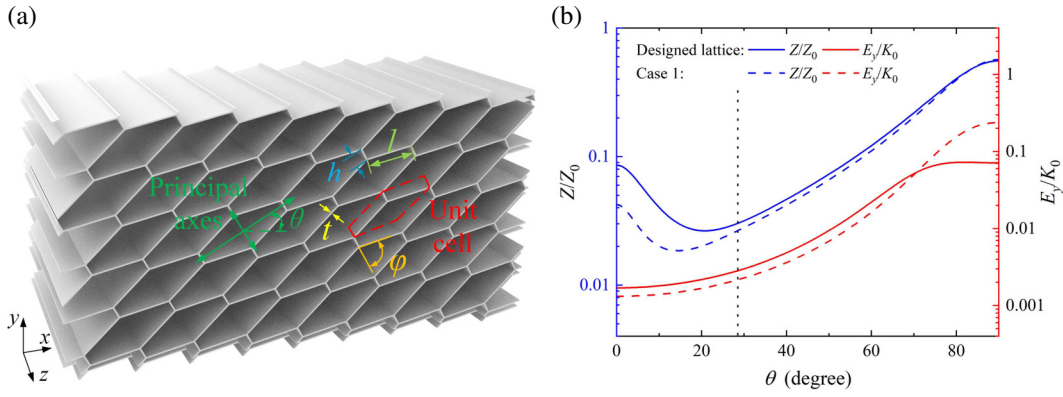


FIG. 6. (a) Characteristics of anisotropic honeycomb lattice, and (b) relative impedance and modulus of the designed anisotropic lattice as a function of θ .

illustrate the advantage of anisotropic materials in shaping the impedance and resistance modulus, we scan the parameters within the scope of optimization for both anisotropic materials and isotropic materials. The resulting regions of attainable values for impedance and modulus are depicted in Fig. 5(d), which vividly highlights a broader design space for anisotropic materials over isotropic ones.

B. Microstructure design of low-impedance anisotropic materials

An ideal anisotropic pentamode material is unstable due to the internal mechanism, so in practice, it can be well approximated by utilizing a compliant mechanism [33]. More concretely, we choose a configuration of an anisotropic honeycomb lattice as a basis; this is characterized by three dimensionless parameters: the length ratio h/l , dimensionless thickness t/l , and topology angle φ , as illustrated in Fig. 6(a) [29]. The lattice is extruded along the z axis, making the loading capacities along the extrusion direction much stronger than those in the easy deformation plane (x - O - y). This characteristic makes the lattice well subjected to the plane-strain assumption. The

size of the lattice cell is set to $l = 10$ mm to ensure a sufficient number of cells within the test sample. Aluminum with a mass density of 2700 kg/m³, Young's modulus of 69 GPa, and Poisson ratio of 0.33 is used as the lattice material. The geometric parameters of the microstructure are optimized based on the homogenization of the lattice [33]. The detailed procedure is provided in Appendix E. The geometric parameters of the optimal material for case 1 are retrieved as $\varphi = 78^\circ$, $h = 1.5$ mm, and $t = 0.2$ mm. However, considering practical manufacturing capabilities, especially the challenges associated with producing extremely thin beams, we finely tune these parameters as $h = 2.5$ mm and $t = 0.3$ mm, with an approximate homogenized elastic matrix $C_{11} = 1.72K_0$, $C_{12} = 0.26K_0$, $C_{22} = 0.041K_0$, and $C_{66} = 0.006K_0$. With these parameters, the impedance and modulus as a function of θ are illustrated Fig. 6(b), showing a profile similar to the optimized one in case 1. Processability has been improved at the cost of increasing impedance and decreasing modulus.

Targeting an average sound insulation of 20 dB across the low-mid-frequency range, we choose $\theta = 28^\circ$ as a compromise between low impedance and high modulus, as indicated by the dotted black line in Fig. 6(b).

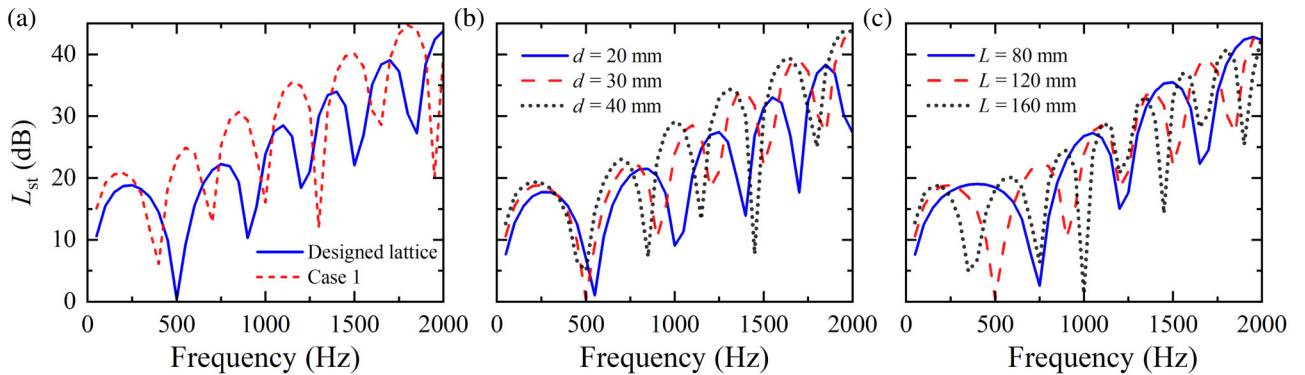


FIG. 7. (a) STL of the silencer with the designed lattice. Effects of (b) thickness and (c) length of the anisotropic lattice plates on STL.

The acoustic performance of STL for the silencer made of such an anisotropic lattice is calculated using the proposed theoretical model and illustrated in Fig. 7(a), which is slightly inferior to the optimal material in case 1. In addition to impedance, the geometric parameters of silencers also significantly influence sound insulation; their effects on STL are illustrated in Figs. 7(b) and 7(c). Thickness d affects the peak values of STL, while length L determines the span of the domelike STL curves. These effects can be approximately explained through the simplified model discussed previously. According to Eq. (13), the axial wave number increases with d (or y_3), therefore amplifying the mismatch of the wave number. Additionally, as indicated by Eq. (11), a larger L results in a smaller k_{xB0} (or frequency) at valleys of the curve. Overall, an increase in the cross-section area of the compliant plates, denoted by $d \times L$, induces a shift in the STL curve towards lower frequencies, and an enhanced performance in the lower-frequency regime.

IV. EXPERIMENTAL VALIDATION

An experimental validation of the designed inline hydraulic silencer made of the anisotropic lattice is conducted and explained in this section. A hydraulic silencer, composed of a cuboid chamber with a cross-section area of $164 \times 164 \text{ mm}^2$ and circular inlet and outlet ports with diameters of $\Phi = 80 \text{ mm}$, is shown in Fig. 8(a). Its shell has a thickness of 10 mm. Two identical anisotropic lattice plates measuring $120 \times 160 \times 30 \text{ mm}^3$ are symmetrically placed to line the chamber. These plates are fabricated using advanced electric discharge machining technology, with the geometric parameters outlined in Sec. III C ($l = 10 \text{ mm}$, $h = 2.5 \text{ mm}$, $t = 0.3 \text{ mm}$), as shown in Fig. 8(b). To protect the lattice structures from water ingress, 2-mm-thick rubber slices are sealed on five sides of the cuboids, as shown in the inlet, only leaving one side—the grounded side in Fig. 8(b)—exposed to water. During the experiment, an acoustic source excites waves in the pipeline, with sensors positioned upstream and downstream of the silencer to collect wave pressures. The resulting STL curve, as plotted in Fig. 9, shows an average of approximately 21 dB across the frequency range of 100 Hz to 2 kHz, demonstrating outstanding sound insulation of this developed hydraulic silencer.

Meanwhile, theoretical predictions are also conducted using the proposed model with anisotropic compliant materials. Considering the rubber coatings, the equivalent material parameters for the sealed plates are evaluated using the equivalent strain-energy method. The modulus of rubber is 28 MPa, as measured by the MTS testing machine. The density and Poisson ratio are 1200 kg/m^3 and 0.49, respectively.

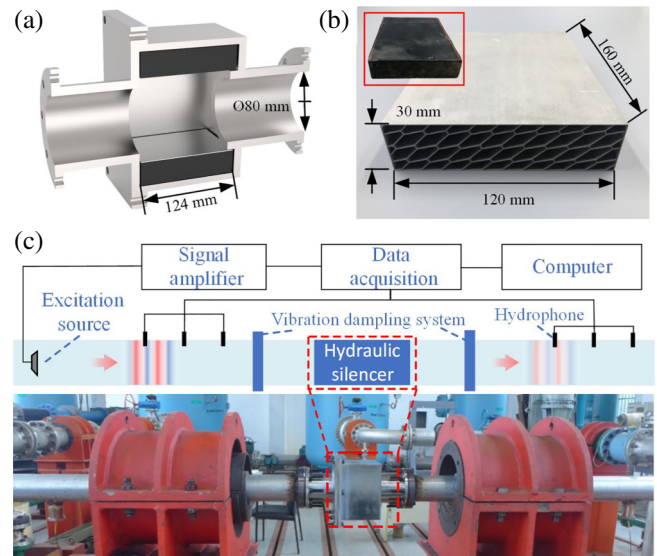


FIG. 8. (a) Cross-section view of the tested silencer. (b) Anisotropic latticed plate in the silencer. (c) Testing system.

Figure 9 shows a comparison between theoretical predictions and experimental results, demonstrating satisfactory agreement. The discrepancies observed are mainly attributed to the following factors. First, the silencer in the experiment includes circular cross sections for the inlet and outlet, which differ from the simplified 2D model. Aspects such as the expansion in the z direction and the protrusion of the inlet pipe are not fully accounted for in the theoretical model. Additionally, assembling errors of the reflective plates may result in a nonideal boundary. Moreover, the steel shell in the experiment may lead to a nonideal acoustic rigid boundary, particularly at low frequencies. Despite these discrepancies and limitations, the

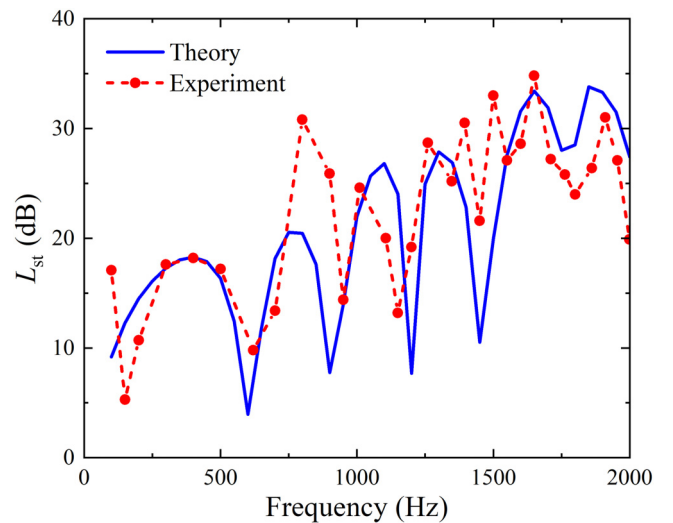


FIG. 9. Comparison between experiments and theoretical predictions of STL.

good correlation observed between theory and experiment validates our innovative design for the hydraulic silencer with anisotropic materials.

V. CONCLUSIONS

An analytical model is developed to predict the performance of inline hydraulic silencers with anisotropic reflective materials. Based on the model, a large material space can be utilized to search for compliant materials. It is found that an extremely anisotropic material with an extremely low quasitransverse wave velocity and a single nonzero normalized eigenvalue (elastic matrix) offers an optimal solution when subjected to a moderate pressure. This kind of material enables the conventional positive correlation between impedance and stiffness found in isotropic materials, possessing low impedance and the required modulus simultaneously, to be broken down. Based on these findings, a lattice of a highly anisotropic compliant material is designed and fabricated to fulfill the stringent requirements of low impedance and necessary modulus. This solid-compliant material is then equipped into a hydraulic silencer, and its performance is measured experimentally. The measured results demonstrate an average STL of 21 dB across a frequency range of 100 to 2000 Hz, aligning closely with the predictions of the proposed model. The work enables reflective materials to be found outside of isotropic materials, thus significantly broadening the material selection space for reactive hydraulic silencers and paving the way for innovative solutions to noise reduction.

ACKNOWLEDGMENTS

This work was supported by the National Natural Science Foundation of China (Grants No. 12202054, No. 11632003, No. 11972083, and No. 11991030).

APPENDIX A: DISPLACEMENTS IN ANISOTROPIC PLATES

The anisotropic plates in region D are supposed to be an orthotropic material with density ρ_s . Its 2D constitutive equation in the global coordinate x - O - y is

$$\begin{Bmatrix} \sigma_x \\ \sigma_y \\ \sigma_{xy} \end{Bmatrix} = \begin{bmatrix} C_{11} & C_{12} & C_{16} \\ C_{12} & C_{22} & C_{26} \\ C_{16} & C_{26} & C_{66} \end{bmatrix} \begin{Bmatrix} \varepsilon_x \\ \varepsilon_y \\ 2\varepsilon_{xy} \end{Bmatrix}, \quad (\text{A1})$$

where σ_x , σ_y , and σ_{xy} are the stress components and ε_x , ε_y , and ε_{xy} are the strain components.

The displacement vector of the n th mode in this anisotropic material is represented by

$$\mathbf{u}_n^+ = \begin{Bmatrix} u_{xn}^+ \\ u_{yn}^+ \end{Bmatrix} = \sum_{\alpha=1}^4 I_{Bn} u_{n\alpha}^+ \begin{Bmatrix} m_{n\alpha}^+ \\ n_{n\alpha}^+ \end{Bmatrix} e^{-j(k_x B_n x + k_y \alpha n y)}, \quad (\text{A2})$$

where $u_{n\alpha}^+$ is the amplitude and $\{m_{n\alpha}^+, n_{n\alpha}^+\}^T$ is the normalized polarization vector. The superscript “+” in this expression denotes the forward incident waves. Unlike isotropic materials, the polarization depends on incidence direction for anisotropic materials, allowing for a more subtle way to manage acoustic waves.

By solving the Christoffel equation, $-\omega^2 \rho_s \mathbf{u}_n^+ = \nabla \cdot \boldsymbol{\sigma}$, where $\boldsymbol{\sigma} = [\sigma_x, \sigma_{xy}; \sigma_{xy}, \sigma_y]$, the vertical components of different wave numbers $k_{y\alpha}$ ($\alpha = 1-4$) are obtained. The fluid-solid boundary conditions at the interface ($y = y_2$) yield

$$\begin{aligned} \frac{j}{\rho_0 \omega} \frac{\partial P_B^+}{\partial y} &= j \omega u_{yn}^+, \\ -P_B^+ &= C_{12} \frac{\partial u_{xn}^+}{\partial x} + C_{22} \frac{\partial u_{yn}^+}{\partial y} + C_{26} \left(\frac{\partial u_{xn}^+}{\partial y} + \frac{\partial u_{yn}^+}{\partial x} \right) \quad (\text{A3}) \\ C_{16} \frac{\partial u_{xn}^+}{\partial x} + C_{26} \frac{\partial u_{yn}^+}{\partial y} + C_{66} \left(\frac{\partial u_{xn}^+}{\partial y} + \frac{\partial u_{yn}^+}{\partial x} \right) &= 0. \end{aligned}$$

The boundary condition at the rigid boundary ($y = y_3$) gives

$$u_{xn}^+(x, y_3) = 0, \quad u_{yn}^+(x, y_3) = 0. \quad (\text{A4})$$

Combining Eqs. (A1)–(A4), the axial wave number k_{xBn} can be calculated for a given frequency. Following a similar process, the displacements and their corresponding wave numbers for the backward incident waves can be derived accordingly. Then, the total displacement components are finally expressed as

$$\begin{aligned} \mathbf{u}_n &= \sum_{\alpha=1}^4 I_{Bn} u_{n\alpha}^+ \begin{Bmatrix} m_{n\alpha}^+ \\ n_{n\alpha}^+ \end{Bmatrix} e^{-j(k_x B_n x + k_y \alpha n y)} \\ &+ R_{Bn} u_{n\alpha}^- \begin{Bmatrix} m_{n\alpha}^- \\ n_{n\alpha}^- \end{Bmatrix} e^{j(k_x B_n x + k_y \alpha n y)}, \quad (\text{A5}) \end{aligned}$$

where the superscript “−” denotes the terms excited by the backward incident waves. From the Christoffel equation, it can be shown that the wave numbers in the anisotropic solid associated with the backward incident wave are exactly the opposite of those corresponding to the forward incident waves.

APPENDIX B: DERIVATION OF THE GOVERNING EQUATION

Using the derived expressions for pressure and displacements, the axial particle velocities in both the fluid and

anisotropic material can be readily derived:

$$\begin{aligned}
v_{Ax}(x, y) &= \frac{k_{xA0}}{\rho_0 \omega} I_{A0} e^{-j k_{xA0} x} \psi_{A0}(y) \\
&\quad - \sum_{n=0}^{\infty} \frac{k_{xA_n}}{\rho_0 \omega} R_{A_n} e^{j k_{xA_n} x} \psi_{A_n}(y), \\
v_{Bx}(x, y) &= \sum_{n=0}^{\infty} \frac{k_{xB_n}}{\rho_0 \omega} (I_{B_n} e^{-j k_{xB_n} x} - R_{B_n} e^{j k_{xB_n} x}) \psi_{B_n}(y), \\
v_{Cx}(x, y) &= \sum_{n=0}^{\infty} \frac{k_{xC_n}}{\rho_0 \omega} I_{C_n} e^{-j k_{xC_n} x} \psi_{C_n}(y), \\
v_{Dx}(x, y) &= \sum_{n=0}^{\infty} j \omega [I_{B_n} e^{-j k_{xB_n} x} \psi_{D_n}^+(y) \\
&\quad + R_{B_n} e^{-j k_{xB_n} x} \psi_{D_n}^-(y)],
\end{aligned} \tag{B1}$$

where $\psi_{D_n}^{\pm}(y) = \sum_{\alpha=1}^4 m_{\alpha n}^{\pm} u_{\alpha n}^{\pm} e^{\mp j k_{y\alpha n} y}$ represents the transverse mode of the plate.

The pressure continuity with the weighted integration at $x = 0$ between regions A and B is represented as

$$\begin{aligned}
&\sum_{n=0}^N (I_{A_n} + R_{A_n}) \int_0^{y_1} \psi_{A_n}(y) \psi_{B_s}(y) dy \\
&= \sum_{n=0}^N (I_{B_n} + R_{B_n}) \int_0^{y_1} \psi_{B_n}(y) \psi_{B_s}(y) dy,
\end{aligned} \tag{B2}$$

where $s = 0, 1, \dots, N$. The wave components are truncated to order N .

The continuity of the velocity with the weighted integration results in

$$\begin{aligned}
&\sum_{n=0}^{\infty} k_{xA_n} (I_{A_n} - R_{A_n}) \int_0^{y_1} \psi_{A_n}(y) \psi_{B_s}(y) dy \\
&= \sum_{n=0}^{\infty} k_{xB_n} (I_{B_n} - R_{B_n}) \int_0^{y_2} \psi_{B_n}(y) \psi_{B_s}(y) dy \\
&\quad + j \omega^2 \rho_0 \sum_{n=0}^N I_{B_n} \int_{y_2}^{y_3} \psi_{D_n}^+(y) \cdot \frac{j \omega^2 \rho_D}{k_{xB_s}} \psi_{D_n}^+(y) dy \\
&\quad + j \omega^2 \rho_0 \sum_{n=0}^N R_{B_n} \int_{y_2}^{y_3} \psi_{D_n}^-(y) \cdot \frac{j \omega^2 \rho_D}{k_{xB_s}} \psi_{D_n}^+(y) dy,
\end{aligned} \tag{B3}$$

where the weighted function in the solid is chosen as the normalized transversal mode of the plate.

Similarly, the continuity conditions at $x = L$ between regions B and C are provided as follows:

$$\begin{aligned}
&\sum_{n=0}^N (I_{B_n} e^{-j k_{xB_n} L} + R_{B_n} e^{j k_{xB_n} L}) \int_0^{y_1} \psi_{B_n}(y) \psi_{B_s}(y) dy \\
&= \sum_{n=0}^N I_{C_n} \int_0^{y_1} \psi_{C_n}(y) \psi_{B_s}(y) dy, \\
&\sum_{n=0}^N k_{xB_n} (I_{B_n} e^{-j k_{xB_n} L} - R_{B_n} e^{j k_{xB_n} L}) \int_0^{y_2} \psi_{B_n}(y) \psi_{B_s}(y) dy \\
&\quad + j \omega^2 \rho_0 \sum_{n=0}^N I_{B_n} e^{-j k_{xB_n} L} \int_{y_2}^{y_3} \psi_{D_n}^+(y) \frac{j \omega^2 \rho_D}{k_{xB_s}} \psi_{D_n}^+(y) dy \\
&\quad + j \omega^2 \rho_0 \sum_{n=0}^N R_{B_n} e^{j k_{xB_n} L} \int_{y_2}^{y_3} \psi_{D_n}^-(y) \frac{j \omega^2 \rho_D}{k_{xB_s}} \psi_{D_n}^+(y) dy \\
&= \sum_{n=0}^N k_{xC_n} I_{C_n} \int_0^{y_1} \psi_{C_n}(y) \psi_{B_s}(y) dy.
\end{aligned} \tag{B4}$$

$$\tag{B5}$$

Combining Eqs. (B2)–(B5), we get a set of $4(N+1)$ equations, involving $4(N+1)$ unknown coefficients: R_{A_n} , I_{B_n} , R_{B_n} , and I_{C_n} . Here, the amplitude of the incident wave I_{A0} is assumed to be unity.

When the material in region D is an isotropic fluid medium, the corresponding Eqs. (B3) and (B5) are reduced to those in Ref. [9] as

$$\begin{aligned}
&\sum_{n=0}^{\infty} k_{xA_n} (I_{A_n} - R_{A_n}) \int_0^{y_1} \psi_{A_n}(y) \psi_{B_s}(y) dy \\
&= \sum_{n=0}^{\infty} k_{xB_n} (I_{B_n} - R_{B_n}) \int_0^{y_2} \psi_{B_n}(y) \psi_{B_s}(y) dy \\
&\quad + \sum_{n=0}^{\infty} \frac{\rho_B}{\rho_D} k_{xB_n} (I_{B_n} - R_{B_n}) \int_{y_2}^{y_3} \psi_{D_n}(y) \psi_{D_s}(y) dy,
\end{aligned} \tag{B6}$$

where $\psi_{B_n}(y) = C_1 e^{-j k_{yD_n} y} + C_2 e^{j k_{yD_n} y}$ is the transversal mode of region D.

APPENDIX C: SETUP FOR NUMERICAL SIMULATIONS

The STL of the silencer is obtained numerically using COMSOL Multiphysics. A 2D model is established, as shown Fig. 10, employing the pressure acoustic and solid mechanics modules. The pressure acoustic module calculates the pressure variations associated with the propagation of underwater acoustic waves, while the solid

mechanics module analyzes wave propagation in solid-compliant materials. Acoustic structure boundary conditions [indicated by the dashed green lines in Fig. 10] are applied at the solid-fluid interfaces (continuity on velocity and pressure). Plane-wave radiation boundary conditions (the blue lines) are set at the inlet and outlet. The fixed (zero displacement, indicated by the red lines) and roller (zero normal displacement, indicated by dotted red lines) boundary conditions are imposed on the back and side boundaries of the solid materials, respectively. Other boundaries (black lines) of the pipeline are considered to be acoustically rigid walls, i.e., sound hard boundaries. The STL of the silencer can be determined as

$$L_{\text{st}} = -20 \log_{10} \frac{P_{\text{tr}}}{P_{\text{in}}}, \quad (\text{C1})$$

where P_{in} and P_{tr} denote the amplitudes of the incident and transmitted waves, respectively.

APPENDIX D: OPTIMIZATION OF ANISOTROPIC COMPLIANT MATERIALS

A parameter-sweeping analysis is employed to determine the optimal elastic parameters C_{11} , C_{12} , C_{22} , and C_{66} and rotational angle θ of the compliant material. The design objective is to maximize the average STL values within the frequency range of 100 Hz to 2 kHz (with 100 Hz intervals). The search ranges for these elastic parameters are set between $0.005K_0$ and $3K_0$, while θ is confined to a range from 0° to 90° . Additionally, to ensure adequate pressure resistance against hydrostatic pressure, a constraint on the minimum vertical modulus is also imposed as

$$E_y = 1/\mathbf{C}^{-1}(2,2) \geq \bar{E}_y, \quad (\text{D1})$$

where E_y is the normalized modulus along the y axis. \bar{E}_y is the desired pressure-resistance capacity. The mathematical formula of this optimization process can be expressed as

$$\begin{aligned} &\text{Find } [C_{11}, C_{12}, C_{22}, C_{66}, \theta], \\ &\text{Max. average } (L_{\text{st}}), \\ &\text{S.t. } E_y \geq \bar{E}_y. \end{aligned} \quad (\text{D2})$$

APPENDIX E: DESIGN OF THE HONEYCOMB LATTICE

In Ref. [33], a numerical homogenization method for the honeycomb is established to link the geometric parameters of the lattice and the homogenized elastic matrix. Following this method, a parameter-sweeping analysis is conducted to determine the geometrical parameters for the desired homogenized material.

A 2D model of a honeycomb lattice cell is constructed in COMSOL Multiphysics using the solid mechanics module. Bloch boundary conditions are applied to the opposite sides of the lattice. In a 2D Cartesian coordinate system aligned with the principal axes, the homogenized elastic matrix can be expressed by

$$\mathbf{C} = \begin{bmatrix} C_{11} & C_{12} & 0 \\ C_{12} & C_{22} & 0 \\ 0 & 0 & C_{66} \end{bmatrix}. \quad (\text{E1})$$

From this effective elasticity matrix and the effective mass density, the phase velocities of elastic waves propagating along different directions can be derived using the Christoffel equation. To retrieve the elastic matrix, specific wave-propagation directions are selected, and the corresponding velocities are calculated numerically from the band diagram. By equating the phase velocities obtained from the band diagram to those estimated by the effective elastic matrix, this enables us to determine the effective elastic constants.

For the waves along the x and y axes, purely longitudinal and transversal waves exist, respectively, with the velocities:

$$\begin{aligned} x \text{ direction } c_{Lx}^2 &= C_{11}/\rho_s; & c_{Tx}^2 &= C_{66}/\rho_s, \\ y \text{ direction } c_{Ly}^2 &= C_{22}/\rho_s, \end{aligned} \quad (\text{E2})$$

where c denotes the phase velocity; subscripts “ L ” and “ T ” stand for longitudinal and transverse, respectively, while “ x ” and “ y ” represent the directions. ρ_s is the effective density obtained by averaging the mass within the unit cell.

In the case of the off-axis propagation direction, quasi-longitudinal and quasitransversal waves exist. For example, the velocities of the waves along 45° from the x axis are expressed as

$$\begin{aligned} 45^\circ \text{ direction } c_{qL}^2 &= \frac{1}{4\rho_s} \sqrt{C_{11} + C_{22} + 2C_{66} + \sqrt{(C_{11} - C_{22})^2 + 4(C_{12} + C_{66})^2}}, \\ c_{qT}^2 &= \frac{1}{4\rho_s} \sqrt{C_{11} + C_{22} + 2C_{66} - \sqrt{(C_{11} - C_{22})^2 + 4(C_{12} + C_{66})^2}}. \end{aligned} \quad (\text{E3})$$

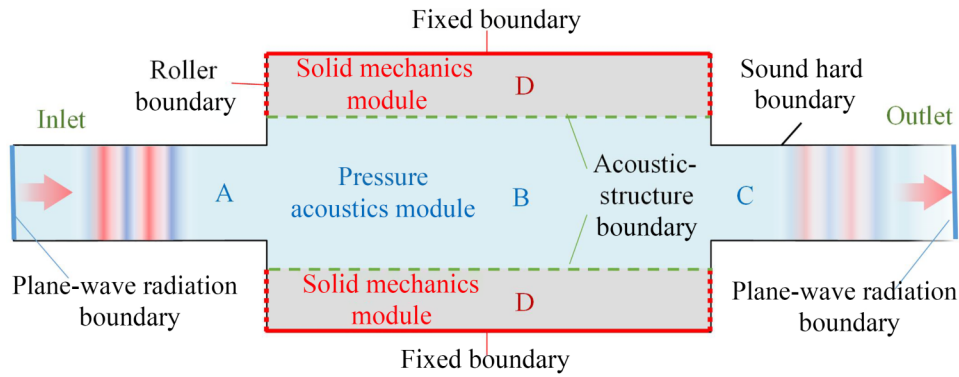


FIG. 10. 2D simulation model of the silencer.

By substituting the numerically calculated velocities from the band diagram, the homogenized elastic constants of the honeycomb lattice can be readily calculated. This method is valid for quasistatic cases without resonance.

Based on this homogenized method, the geometrical parameters of the desired material are determined through a parameter-sweeping analysis. The design process can be established by a minimization procedure:

$$\min_{h,t,\varphi} [(\bar{C}_{11} - C_{11})^2 + (\bar{C}_{22} - C_{22})^2 + (\bar{C}_{12} - C_{12})^2 + (\bar{C}_{66} - C_{66})^2], \quad (\text{E4})$$

where the variables with bars denote the targeted ones. The length of lattice l is chosen to be 10 mm to ensure a sufficient number of cells within the test sample.

- [1] T. Du, S. Li, J. Liu, and D. Wu, Acoustic performance of a water muffler, *Noise Control Eng. J.* **63**, 239 (2015).
- [2] M. Lashkarbolok, Fluid-structure interaction in thin laminated cylindrical pipes during water hammer, *Compos. Struct.* **204**, 912 (2018).
- [3] W. Li, X. Kong, Q. Xu, and Z. Hao, Vibration control and bandgap tuning of layer-gradient periodic pipes based on composite cell, *Compos. Struct.* **338**, 118109 (2024).
- [4] X. Yu, L. Cheng, and X. You, Hybrid silencers with micro-perforated panels and internal partitions, *J. Acoust. Soc. Am.* **137**, 951 (2015).
- [5] F. D. Denia, A. Selamet, F. J. Fuenmayor, and R. Kirby, Acoustic attenuation performance of perforated dissipative mufflers with empty inlet/outlet extensions, *J. Sound Vib.* **302**, 1000 (2007).
- [6] M. B. Xu, A. Selamet, I. J. Lee, and N. T. Huff, Sound attenuation in dissipative expansion chambers, *J. Sound Vib.* **272**, 1125 (2004).
- [7] Z. L. Ji, Boundary element analysis of a straight-through hybrid silencer, *J. Sound Vib.* **292**, 415 (2006).
- [8] L. Shen, Y. Zhu, F. Mao, S. Gao, Z. Su, Z. Luo, H. Zhang, and B. Assouar, Broadband low-frequency acoustic metamuffler, *Phys. Rev. Appl.* **16**, 064057 (2021).
- [9] A. Selamet, M. B. Xu, I. J. Lee, and N. T. Huff, Analytical approach for sound attenuation in perforated dissipative silencers with inlet/outlet extensions, *J. Acoust. Soc. Am.* **117**, 2078 (2005).
- [10] Z. L. Ji, Boundary element acoustic analysis of hybrid expansion chamber silencers with perforated facing, *Eng. Anal. Bound. Elem.* **34**, 690 (2010).
- [11] F. D. Denia, A. Selamet, M. J. Martínez, and F. J. Fuenmayor, Sound attenuation of a circular multi-chamber hybrid muffler, *Noise Control Eng. J.* **56**, 356 (2008).
- [12] H. S. Kim, P. S. Ma, B. K. Kim, S. R. Kim, and Y. H. Seo, Underwater sound absorption and insulation of elastic micro-perforated plates in impedance tubes, *Appl. Acoust.* **197**, 108935 (2022).
- [13] E. R. Gruber, *High-Pressure Compliant Syntactic Foam for Hydraulic Noise Control* (Georgia Institute of Technology, Atlanta, 2016).
- [14] A. Selamet, N. S. Dickey, and J. M. Novak, The Herschel-Quincke tube: A theoretical, computational, and experimental investigation, *J. Acoust. Soc. Am.* **96**, 3177 (1994).
- [15] Z. B. Wang, Y. K. Chiang, Y. S. Choy, C. Q. Wang, and Q. Xi, Noise control for a dipole sound source using micro-perforated panel housing integrated with a Herschel-Quincke tube, *Appl. Acoust.* **148**, 202 (2019).
- [16] H. B. Shao, H. He, Y. Chen, and G. P. Chen, A novel multi-cavity Helmholtz muffler, *Chin. Phys. B* **28**, 064303 (2019).
- [17] X. Wang and C. M. Mak, Wave propagation in a duct with a periodic Helmholtz resonators array, *J. Acoust. Soc. Am.* **131**, 1172 (2012).
- [18] A. Selamet, F. D. Denia, and A. J. Besa, Acoustic behavior of circular dual-chamber mufflers, *J. Sound Vib.* **265**, 967 (2003).
- [19] Z. Fang, Z. L. Ji, and C. Y. Liu, Acoustic attenuation analysis of silencers with multi-chamber by using coupling method based on subdomain division technique, *Appl. Acoust.* **116**, 152 (2017).
- [20] B. H. An and J. W. Lee, Metamaterial-based muffler with broadband tunability in a limited space: optimal design, theoretical investigation and experiment, *Int. J. Mech. Sci.* **205**, 106594 (2021).
- [21] W. A. Altabey, M. Noori, Z. Wu, M. A. Al-Moghazy, and S. A. Kouritem, Studying acoustic behavior of BFRP laminated composite in dual-chamber muffler application using deep learning algorithm, *Materials* **15**, 8071 (2022).

- [22] A. Selamet and Z. L. Ji, Acoustic attenuation performance of circular expansion chambers with extended inlet/outlet, *J. Sound Vib.* **223**, 197 (1999).
- [23] M. Åbom, Derivation of four-pole parameters including higher order mode effects for expansion chamber mufflers with extended inlet and outlet, *J. Sound Vib.* **137**, 403 (1990).
- [24] L. Huang, Broadband sound reflection by plates covering side-branch cavities in a duct, *J. Acoust. Soc. Am.* **119**, 2628 (2006).
- [25] L. Huang, Modal analysis of a drumlike silencer, *J. Acoust. Soc. Am.* **112**, 2014 (2002).
- [26] Y. Xi, B. R. Li, L. L. Gao, T. F. Tang, and H. L. Liao, Acoustic attenuation performance prediction and analysis of bladder style hydraulic noise suppressors, *Appl. Acoust.* **134**, 131 (2018).
- [27] N. Pedigo and K. A. Cunefare, in INTER-NOISE and NOISE-CON Congress and Conference Proceedings, Institute of Noise Control Engineering (2018), Vol. 258, pp. 3442–3449.
- [28] B. Zhao, D. Wang, P. Zhou, X. Liu, and G. Hu, Design of load-bearing materials for isolation of low-frequency waterborne sound, *Phys. Rev. Appl.* **17**, 034065 (2022).
- [29] Y. Chen, B. Zhao, X. Liu, and G. Hu, Highly anisotropic hexagonal lattice material for low frequency water sound insulation, *Extreme Mech. Lett.* **40**, 100916 (2020).
- [30] Y. Wang, H. Zhao, H. Yang, J. Liu, D. Yu, and J. Wen, Topological design of lattice materials with application to underwater sound insulation, *Mech. Syst. Signal Process.* **171**, 108911 (2022).
- [31] L. E. Kinsler, A. R. Frey, A. B. Coppens, and J. V. Sanders, *Fundamentals of Acoustics* (John Wiley & Sons, New York, 2000).
- [32] M. F. Gross, J. L. G. Schneider, Y. Wei, Y. Chen, S. Kalt, M. Kadic, X. Liu, G. Hu, and M. Wegener, Tetramode metamaterials as phonon polarizers, *Adv. Mater.* **35**, 2211801 (2023).
- [33] Y. Chen, X. Liu, and G. Hu, Latticed pentamode acoustic cloak, *Sci. Rep.* **5**, 15745 (2015).